Author/s:
Zhang, Q;Chang, Z;Xu, G;Wang, Z;Zhang, Y;Xu, ZQ;Chen, S;Bao, Q;Liu, JZ;Mai, YW;Duan, W;Fuhrer, MS;Zheng, C

Title:
Strain Relaxation of Monolayer WS2 on Plastic Substrate

Date:
2016-12-20

Citation:
Zhang, Q., Chang, Z., Xu, G., Wang, Z., Zhang, Y., Xu, Z. Q., Chen, S., Bao, Q., Liu, J. Z., Mai, Y. W., Duan, W., Fuhrer, M. S. & Zheng, C. (2016). Strain Relaxation of Monolayer WS2 on Plastic Substrate. Advanced Functional Materials, 26 (47), pp.8707-8714. https://doi.org/10.1002/adfm.201603064.

Persistent Link:
https://hdl.handle.net/11343/291883

DOI: adfm.201603064

Article type: Full Paper

Strain Relaxation of Monolayer WS_2 on Plastic Substrate

Qianhui Zhang, Zhenyue Chang, Guanzhong Xu, Ziyu Wang, Yupeng Zhang, Zai-Quan Xu, Shujian Chen, Qiaoliang Bao, Jefferson Zhe Liu, Yui-Wing Mai, Wenhui Duan, Michael S. Fuhrer*, Changxi Zheng**

Q. Zhang, G. Xu, S. Chen, W. H. Duan, C. Zheng

Department of Civil Engineering

Monash University

Clayton, VIC 3800 Australia

E-mail: wenhui.duan@monash.edu, changxi.zheng@monash.edu

Z. Chang, J. Z. Liu

Department of Mechanical Engineering

This is the author manuscript accepted for publication and has undergone full peer review but has not been through the copyediting, typesetting, pagination and proofreading process, which may lead to differences between this version and the Version of Record. Please cite this article as doi: 10.1002/adfm.201603064.

This article is protected by copyright. All rights reserved.

Monash University

Clayton, VIC 3800 Australia

Z. Wang, Y. Zhang, Z. Q. Xu, Q. Bao

Department of Materials Science and Engineering

Monash University

Clayton, VIC 3800 Australia

Q. Bao, W. H. Duan, Prof. M. S. Fuhrer, C. Zheng

Monash Centre for Atomically Thin Materials

Monash University

Clayton, VIC 3800 Australia

E-mail: michael.fuhrer@monash.edu

Prof. Y. W. Mai

Centre for Advanced Materials Technology (CAMT), School of Aerospace, Mechanical and Mechatronic Engineering J07

The University of Sydney

Sydney, NSW 2006, Australia

Keywords: Strain relaxation, transition metal dichalcogenides, exciton, trion, and finite element simulation

Abstract

Strain-dependent electrical and optical properties of atomically thin transition metal dichalcogenides may be useful in sensing applications. However, the question of how strain relaxes in atomically thin materials remains not well understood. Herein we investigate the strain relaxation of triangular WS_2 deposited on polydimethylsiloxane (PDMS) substrate. The photoluminescence of trions (X^-) and excitons (X^0) undergo linear redshifts of ~20 meV when the substrate tensile strain increases from 0 to 0.16. However, when the substrate strain further increases from 0.16 to 0.32, the redshifts cease due to strain relaxation in WS_2. The strain relaxation occurs through formation of wrinkles in the WS_2 crystal. The pattern of wrinkles is found to be dependent on the relative angle between an edge of the triangular WS_2 crystal and tensile strain direction. Finite element simulations of the strain distribution inside the WS_2 crystals explain our experimental observations.

1. Introduction

Semiconducting transition metal dichalcogenides (TMDs) of family (Mo,W) $(S,Se)_2$ recently have been intensively studied for their superior properties and attractive potential applications. Firstly, TMDs undergo indirect to direct bandgap transition when thinning down to monolayer.[1] The direct bandgap gives TMDs strong light absorption and photoluminescence (PL). Secondly, atomically thin TMDs are strongly covalently bonded yet have chemically inert van der Waals surfaces. Thus, TMDs are stable in various environment, and demonstrate extremely small bending rigidity κ and exceptionally high Young's modulus.[2-4] Thirdly, monolayer TMDs show piezoelectricity due to the broken inversion symmetry.[5, 6] As a result, monolayer TMDs indicate significant potential for flexible optoelectronics,[7, 8] piezotronics,[5, 6] mechanically enhanced nanocomposites[9] and smart materials for strain sensing.[10] In these applications, strain is inevitably a critical object requiring comprehensive understanding.

So far, substantial efforts have been spent on the study of strain engineering to the band structure of TMDs by using bending,[11-15] high pressure compression,[16-24] and tensile elongation.[25] Their results indicate strain is an effective way to tune the bandgap from direct to indirect, generate the redshifts of trion and exciton peaks, and change the material conductivity from semiconducting to metallic.[26] However, an important question of how strain relaxes inside TMDs is still an open question.

This article is protected by copyright. All rights reserved.

Herein, we investigate the strain relaxation of monolayer WS_2 triangular crystals deposited on polydimethylsiloxane (PDMS) substrate. The uniaxial tensile strain applied to the WS_2 crystals is transferred from PDMS substrate when the substrate is elongated by a loading frame. We observe that the trion and exciton PL peaks undergo redshift when the substrate strain is increased from 0 to 0.16. However, the redshifts stop when the substrate strain is further increased from 0.16 to 0.32. This is caused by the strain relaxation in WS_2 through the formation of wrinkles across the crystals. The wrinkle distribution is found to be drastically different when the angle between an edge of the triangular WS_2 crystal and the substrate elongation direction changes. The morphology of wrinkles is characterized by atomic force microscopy. These experimental observations can be well explained by finite element (FE) simulations.

2. Results and Discussion

Chemical vapour deposition (CVD) is applied to grow high quality WS_2 crystals on atomically flat $Al_2O_3(0001)$ using WO_3 and S powders as the precursors, see Figure S1 and Experimental Section. In brief, the powders are located into the middle (WO_3) and upstream (S) of a 25 mm quartz tube, and heated by furnace and heating tape to 800 °C and 200 °C in 0.5 h, respectively. Monolayer WS_2 is grown on sapphire substrates by maintaining the temperatures for 0.25 h. Figure S2a-c shows the optical image and AFM topography of a representative grown WS_2 crystal on sapphire. The zoomed-in AFM image shown in Figure S2c indicates the atomic flatness of WS_2 crystals grown on the terraces of sapphire(0001). Edges of the triangle WS_2 crystal are raised in height due to water intercalation into the interface between WS_2 and the hydrophilic sapphire substrate.[27] Scanning PL images taken under 532 nm excitation indicate uniform PL and Raman signals across the WS_2 crystal except extraordinary PL intensity at the edges, see Figure S2d-f. We infer the extraordinary PL intensity at the edges is related to the intercalated water based on the AFM image.[27] It should be noticed that the uniform PL peak energy image shown in Figure S2f is obtained by using single peak Lorentzian fitting to the mapped PL spectra.

Figure S2g shows the PL spectrum of the WS_2 crystal on the sapphire growth substrate. A fit of the spectrum (blue line) indicates two Lorentzian peaks identified as due to the trion (X^-, 1.972 eV, green line) and exciton (X^0, 1.991 eV, red line) with 19 meV difference. The peak intensity ratio of exciton to trion is ~2.0, close to WS_2 or MoS_2 on SiO_2/Si with 10 V gate voltage which is at negative doping.[28, 29] We therefore deduce the trion binding energy should be ≤19 meV since the energy difference between X^- and X^0 increases as the negative doping going up.[28, 30] The energies of trion binding as well as the X^- and X^0 peak energies are much smaller compared to those observed for WS_2 on SiO_2/Si,[28] possibly due to the larger dielectric constant of Al_2O_3. Owing to the weak laser power (50 μW) of 532 nm excitation, the Raman spectrum taken from the WS_2 crystal only indicates the E' peak without showing the A_1' peak, see Figure S2h.

For the purpose of strain measurement, CVD grown WS_2 crystals are transferred to PDMS substrates by PMMA-assisted wet transfer method, see Experimental Section and Figure S3. **Figure**

1a-c shows the optical image and AFM topography mapping of the same WS_2 crystal presented in Figure S2 after being transferred on PDMS. The flake is rotated due to the transfer process. It can be seen that the transferred crystal remains intact and clean except for serration of the edges and the appearance of a few wrinkles; see zoomed-in topography image in Figure 1c. The bulk of the crystal is unaffected by the transfer process. The serration of the edges points to defects along the edges as active locations for KOH etching of the WS_2 crystal, while no KOH etching is observed on the main body of WS_2 crystal, indicating a lack of substantial defects. It should be noticed that the extraordinary PL intensity around the edges of WS_2 disappears after being transferred to PDMS, see Figure 1e. The disappearance should be caused by the combination of KOH etching to the edge and the inability of water intercalating the space between WS_2 and hydrophobic PDMS.[27] Also, the PL intensity decreases from edge to centre after being transferred. This feature is observed on intact CVD-grown WS_2 as well due to the chemical heterogeneity.[31, 32] We therefore believe our transferred crystals remain high in quality comparable to those before being transferred. Especially the uniform Raman (Figure 1d) and PL peak position signal (Figure 1f) across the crystal confirm the quality of the transferred crystals without substantial defects such as cracks and holes.

Figure 1g shows a PL spectrum of the transferred crystal at zero strain (ε = 0, black circle). Fitted by Lorentzian, the PL spectrum is composed of trion X^- (green) and exciton X^0 (red) emission at 1.983 eV and 2.022 eV, respectively, with ~40 meV difference. The peak positions and difference are shifted somewhat relative to the unstrained crystal on sapphire, again possibly due to change in

This article is protected by copyright. All rights reserved.

dielectric environment. The dominance of the X^0 peak, of which the peak intensity is ~7 times higher than that of X^-, indicates PDMS is a clean substrate contributing little doping.[33] The clean substrate is desirable to maintain strong light-matter interaction and achieve a sharp PL peak for sensitive applications, since high doping weakens the PL intensity and broadens the peak width.[28,29,,33] Figure 1i shows the schematic of our strain measurement setup. The WS_2/PDMS substrate can be strongly attached to our homemade loading frame after oxygen plasma treatment to the contact surface of PDMS. The loading frame is designed to fit into our commercial Raman microscopy (WITec, Alpha300 R) for *in situ* optical spectrum measurement of strained crystals.

Using the loading frame to elongate the PDMS substrate, we can apply a uniaxial tensile strain to the WS_2 crystals by strain transfer from the substrate. **Figure 2**a shows a continuously redshifted PL spectra of WS_2 as a function of the substrate strain. Unless otherwise stated, all the strain values given hereafter are PDMS substrate strains which are calculated by the ratio of elongated length to its natural length. The strain in the WS_2 crystals is much smaller than the substrate strain due to the non-uniform strain transfer efficiency. Figure 2b shows that the peak energies of trion and neutral exciton redshift linearly as the substrate strain increases. There is a ~20 meV redshift of the X^o peak when the substrate strain increases from 0 to 0.16. Such 20 meV redshift actually corresponds to 0.02 strain in WS_2 based on the density-functional-theory calculations,[15] indicating that the strain transfer efficiency therefore is ~12% which is close to the efficiency of MoS_2 on PDMS.[25] In contrast to the PL spectra, the Raman E' peak only redshifts

This article is protected by copyright. All rights reserved.

slightly for the same level of strain changes, see Figure 2c. The E' peak only shifts 2.5 cm^{-1}, and is consistent with a linear relationship (Figure 2d) within our measurement precision.

However, both the redshifts of X^o and X^- peaks cease when the tensile strain of PDMS is further increased from 0.16 to 0.33 (**Figure 3**a). In this range, X^o and X^- peaks remain at the same levels (or only tiny redshift) along with fluctuations. To understand the phenomena in detail, Figure 3b-d presents the optical images of the crystal at three critical points: no strain ($\varepsilon = 0$), turning point ($\varepsilon = 0.16$), and maximum strain ($\varepsilon = 0.32$). White dashed rectangles with same size are drawn around the crystal to help identify the subtle shape changes inside WS_2. When the strain is increased from 0 to 0.16, the crystal shows elongation along the y axis (the tensile direction), see Figure 3c. Measuring from the image, the elongation is around 0.027, close to the estimation obtained comparing the PL redshift with DFT calculations.[15] Since the Poisson ratio of WS_2 is ~0.22,[34] the strain of 2D WS_2 crystal along the x axis (the compression direction) is approximately 0.006, which is negligible compared with that in the tensile direction. Therefore, the crystal size remains roughly the same along the compression direction, see Figure 3c. However, when the strain is yet further increased to 0.32, the crystal undergoes obvious shortening along the x axis, while its length remains the same along the y axis (Figure 3d). More surprisingly, wrinkles appear and are distributed uniformly across the whole crystal at 0.32 strain. Based on these observations, we infer the WS_2 crystals at high strain level undergo strain relaxation by forming wrinkles to resist further increase of tensile strain inside WS_2, finally leading to the cut-off of the PL redshift. The wrinkles are

This article is protected by copyright. All rights reserved.

formed due to lateral compression of the PDMS perpendicular to the tensile strain direction. The compressive strain is transferred from PDMS to WS_2 by van der Waals bonding of WS_2/PDMS interface.

Furthermore, we find the wrinkle patterns are strongly dependent on the orientation of WS_2 crystals relative to the tensile (elongation) direction. **Figure 4** presents a number of wrinkle patterns formed inside the WS_2 crystals with different orientations and sizes. For better comparison, we replot Figure 3d in Figure 4a. As shown, wrinkles are formed uniformly across the crystal (Figure 4a) when an edge of triangular WS_2 is parallel to the y axis (the tensile direction). However, when an edge is perpendicular to the y axis, the wrinkle formation is much more localized (Figure 4b, c). In addition to the formation of wrinkles, another type of strain relaxation behaviour, rupture, is observed for a larger triangular crystal when under tensile stress. As shown in Figure 4d, a larger triangular crystal breaks into three pieces by forming two parallel cracks. We expect that this is because the larger contact area between WS_2 and PDMS increases the level of the tensile strain transferred to the WS_2 such that its fracture strain is exceeded. Along with these cracks, there are wrinkles forming inside the three broken pieces of WS_2. While the triangular piece shows localized wrinkles, the other two pieces indicate uniform wrinkles inside. The results also suggest shape-dependent wrinkle formation.

To further study the evolution of wrinkles, AFM topography scanning and Raman and PL mapping during tensile strain application are performed. **Figure 5** shows the characterization of

This article is protected by copyright. All rights reserved.

wrinkles on a WS_2 crystal orienting with one edge almost parallel to the tensile direction. From the optical and AFM height images shown in Figure 5a-d, it can be seen that the wrinkles evolve relatively uniformly across the crystal when strain increases from 0.13 to 0.23. The formation of wrinkles start at 0.13 strain rather than 0.16, possibly due to the weaker adhesion between WS_2 and PDMS of this sample. In Figure 5e, AFM height profiles at different strain levels are extracted correspondingly along the yellow lines in Figure 5b,d to reveal the geometry and the development of wrinkles as PDMS strain increases. The vertical axis of the height profiles indicated in Figure 5e are shifted for better comparison. It can be seen that the height of wrinkles grow as the substrate strain increases from 0.13 to 0.23. An example is shown where the height of a wrinkle grows from 6.0 nm to 10.8 nm when strain increases from 0.13 to 0.23. The wrinkles under 0.23 substrate strain are also reflected by Raman and PL mapping, see Figure 5f and g. Figure 5h shows the PL spectra on (Point A) and off (Point B) a wrinkle, respectively . The observation of red-shifted PL both on and off the wrinkles indicates that they remain strained (elongated) along the tensile direction. Lorentzian fitting of the peaks shows that the PL peaks of wrinkle undergo slight red shift relative to those of flat region (off wrinkle). This small additional red shift on the wrinkles indicates a slightly larger strain on the wrinkles compared to off, due to bending. Accordingly, for the crystal with an edge perpendicular to the tensile strain direction, the formation of the wrinkles is much more localized, see Figure S4a-d, f and g. The wrinkles tend to develop from the crystal edge perpendicular to the tensile direction. Height growth of the wrinkles with increasing strain is shown in Figure S4e. Figure S4h indicates similar Raman and PL spectra variations of the wrinkled crystal.

Recently, Liu *et al.* observed non-uniform strain distribution in strained MoS_2 on PDMS using scanning PL microscopy.[25] In their study, an edge of the triangular MoS_2 crystal is perpendicular to the y axis, the same geometry as Figure 4b-d. Since the wrinkle formation is caused by strain relaxation in WS_2, we hypothesize that the pattern and the distribution of these wrinkles reflect the strain magnitude distribution across the WS_2 crystals. Therefore, the strain is uniform when the wrinkles are distributed uniformly such as the case of a crystal edge parallel to the y axis.

To understand the influence of crystal orientation on the strain relaxation behaviour inside WS_2, FE simulation[25] is applied to model the strain distribution inside WS_2 for the cases of the crystal edge perpendicular or parallel to the y axis (the tensile direction). **Figure 6**a,b shows the optical image of a triangular WS_2 crystal with an edge parallel to the tensile direction and the corresponding FE modelling geometry, respectively. Since the crystal has mirror symmetry, we create a mirror plane in our FE model along the white dash line (Figure 6a) to save computation time. Figure 6c,d shows the simulation results at tensile strains of 0.1 and 0.5. In general, the strains are distributed relatively uniformly across the crystal even at 0.5 substrate strain. Similarly, Figure 6e-h shows the optical image, modelling geometry and simulation results of the triangular crystal with an edge perpendicular to the y axis. As shown, the strain distribution becomes highly uneven when the substrate strain is at 0.5 (Figure 6h). While top region of the crystal has tensile strains, the bottom region along the long edge suffers compressive strains. Therefore, the simulation results match well with our experimental data shown in Figure 4, Figure 5 and Figure S4, confirming our

This article is protected by copyright. All rights reserved.

hypothesis that the formation of wrinkles occurs in the regions of highest strain: the pattern of wrinkles reflects the distribution of strain within the WS_2.

After release of the applied tensile strain, most of the wrinkles along the tensile strain direction (y axis) disappear, see Figure S5a-h. In contrast, large amount of wrinkles appear along *x* direction due to the compression caused by the strain released of PDMS substrate. As mentioned, the strain transfer rate from substrate to WS_2 crystals is only ~12%. Thus, there must be sliding between WS_2 and PDMS during substrate elongation. Also the residue wrinkles along y direction indicate sliding along y. Figure S5i-j show the PL spectra at positions of lateral wrinkle (A) and flat region (B) respectively, as indicated in Figure S5b. Lorentzian fitting of PL spectra peaks shows trion peaks at 1.973 eV (A, on wrinkle) and 1.978 eV (B, flat region), along with exciton peaks at 2.018 eV (A, on wrinkle) and 2.022 eV (B, flat region), respectively. The PL peaks on formed wrinkles undergo small red shift (~5 meV) compared with those on flat region. The values, especially peaks at flat region of the released crystal, are close to the peak values of transferred WS_2 on PDMS with zero strain.

3. Conclusion

In summary, we study the response of the optical spectra of monolayer WS_2 to tensile strain by elongating the PDMS substrate on which the transferred WS_2 crystals sit. Our experiments indicate that the WS_2 crystals undergo linear redshifts of X^o and X^- peaks in PL and the E' peak in

Raman, when the uniaxial tensile strain of PDMS substrate is increases from 0 to 0.16. However, we observe the strain relaxation of WS_2 in forming wrinkles and cracks (in large crystals) when the substrate strain is further increased from 0.16 to 0.32. More interestingly, the wrinkle patterns are found to depend on the crystal orientation relative to the tensile strain direction. While the wrinkles are distributed uniformly across the triangular WS_2 crystal with an edge parallel to the tensile direction, localized wrinkles are formed inside the crystal with an edge perpendicular to the tensile direction. These observations are explained by our FE simulations which indicate that the pattern of wrinkling reflects the pattern of strain distribution within each crystal. Our results indicate that for 2D TMD materials to be employed in stretchable electronics field, linear relationship between optical spectral shift to tensile strain only applies when tensile strain are small. Beyond a critical strain value, a new relationship must be established for correct strain indication taking into consideration wrinkle formation. Also, triangular TMD crystals with one edge oriented parallel to the tensile strain direction are preferred for straintronics due to more uniform strain distribution. Our results will help understand the mechanical properties of TMD crystals and shed light on the design of high quality straintronics and flexible electronics.

4. Experimental Section

CVD growth: WS_2 crystals were grown by chemical vapor deposition (CVD) on atomically flat sapphire substrates. The schematic of the method is illustrated in Figure S1. The precursors were WO_3

powders (Sigma-Aldrich, 2.0 g) and sulfur (Sigma-Aldrich, 1 g). Sapphire substrates were cleaned by 10 min sonication in acetone and isopropanol. The growth was performed in a 25 mm quartz tube flowing ultra-high purity hydrogen (10 sccm) and argon (200 sccm) at atmospheric pressure. Sapphire substrates and WO_3 were loaded into separate quartz crucibles and located at the center and downstream of the furnace, respectively. While the sulfur powder was positioned upstream of the WO_3 and heated by a heating tape, the substrates and WO_3 powder were heated by the furnace. The temperature of the furnace and sulfur climbed up to 800 ℃ and 200 ℃ respectively in 0.5 h, maintained for 0.25 h, thereafter cooled down to 500 ℃ quickly. The thickness of the crystals was determined by optical contrast as well as signatures of photoluminescence and Raman scattering.

WS_2 transfer: As shown in Figure S3, the transfer of grown WS_2 from sapphire to PDMS was performed by PMMA-assisted wet transfer technique. PMMA (A6) was spin coated by 500 rpm for 15 s then 3000 rpm for 60 s on the surface of as grown WS_2-sapphire sample, followed by 80 ℃ soft bake for 3 min. Then the PMMA coated WS_2-sapphire sample was soaked into 3 M potassium hydroxide (KOH) solution and kept at 100 ℃ for 2 h. After soaking, the PMMA film with WS_2 crystals was separated from the sapphire by surface tension of DI water and washed to remove the KOH residues. The rinsed WS_2/PMMA film was then fished out by PDMS and baked for 10 to 15 minutes to evaporate the water trapped between the PMMA film and PDMS. Finally, the PMMA film was removed by acetone and IPA rinsing.

Optical and AFM measurements: Raman/PL measurements were performed using a confocal microscope system (WITec alpha 300R) with a 50× objective lens. A 532 nm laser was used to excite samples placed on the loading frame. The spectra were collected using a 600 line/mm grating. To avoid sample damage, 50 μW laser power and 1 s integration time were applied during PL and Raman mapping. The PL intensity images were obtained by summing the PL intensity from 590 nm to 660 nm. The PL peaks of natural and charged excitons were estimated from Lorentzian fitting. The AFM measurement was carried out on Bruker Dimension Icon in tapping mode.

FE simulation: The FE simulation of monolayer WS_2/PDMS model under tension was performed by ABAQUS (version 6.12). The model with WS_2 thickness of 20 μm consists of 30315 nodes and 27709 elements and the model with WS_2 size of 5 μm consist of 19135 nodes and 17107 elements. Perfect bonding was assumed as the interface between monolayer WS_2 and underlying PDMS in the model. Appropriate boundary conditions were applied along the edges of the specimen to simulate uniaxial tensile test. The material properties of Young's modulus and Poisson's ratio adopted in the simulation are 350 kPa and 0.5 for PDMS, and 300 GPa and 0.3 for WS_2.

Supporting Information

Supporting Information is available from the Wiley Online Library or from the author.

Acknowledgements

C.Z. acknowledges support from ARC DECRA (DE140101555). M.S.F. acknowledges support from ARC (DP150103837 and FL120100038). This work was performed in part at the Melbourne Centre for Nanofabrication (MCN) in the Victorian Node of the Australian National Fabrication Facility (ANFF).

Received: ((will be filled in by the editorial staff))
Revised: ((will be filled in by the editorial staff))
Published online: ((will be filled in by the editorial staff))

References

[1] K. F. Mak, C. Lee, J. Hone, J. Shan, T. F. Heinz, *Phys. Rev. Lett.* **2010**, *105*, 136805.

[2] A. Castellanos-Gomez, M. Poot, G. A. Steele, H. S. J. van der Zant, N. Agraït, G. Rubio-Bollinger, *Adv. Mater.* **2012**, *24*, 772.

[3] K. Liu, Q. Yan, M. Chen, W. Fan, Y. Sun, J. Suh, D. Fu, S. Lee, J. Zhou, S. Tongay, J. Ji, J. B. Neaton, J. Wu, *Nano Lett.* **2014**, *14*, 5097.

[4] S. Bertolazzi, J. Brivio, A. Kis, *ACS Nano* **2011**, *5*, 9703.

[5] W. Wu, L. Wang, Y. Li, F. Zhang, L. Lin, S. Niu, D. Chenet, X. Zhang, Y. Hao, T. F. Heinz, J. Hone, Z. L. Wang, *Nature* **2014**, *514*, 470.

[6] H. Zhu, Y. Wang, J. Xiao, M. Liu, S. Xiong, Z. J. Wong, Z. Ye, Y. Ye, X. Yin, X. Zhang, *Nat. Nanotechnol.* **2015**, *10*, 151.

[7] G.-H. Lee, Y.-J. Yu, X. Cui, N. Petrone, C.-H. Lee, M. S. Choi, D.-Y. Lee, C. Lee, W. J. Yoo, K. Watanabe, T. Taniguchi, C. Nuckolls, P. Kim, J. Hone, *ACS Nano* **2013**, *7*, 7931.

[8] J. Pu, Y. Yomogida, K.-K. Liu, L.-J. Li, Y. Iwasa, T. Takenobu, *Nano Lett.* **2012**, *12*, 4013.

[9] O. Eksik, J. Gao, S. A. Shojaee, A. Thomas, P. Chow, S. F. Bartolucci, D. A. Lucca, N. Koratkar, *ACS Nano* **2014**, *8*, 5282.

[10] M. A. Bissett, M. Tsuji, H. Ago, *Phys. Chem. Chem. Phys.* **2014**, *16*, 11124.

[11] H. J. Conley, B. Wang, J. I. Ziegler, R. F. Haglund Jr, S. T. Pantelides, K. I. Bolotin, *Nano lett.* **2013**, *13*, 3626.

[12] K. He, C. Poole, K. F. Mak, J. Shan, *Nano lett.* **2013** , *13*, 2931.

[13] C. Zhu, G. Wang, B. Liu, X. Marie, X. Qiao, X. Zhang, X. Wu, H. Fan, P. Tan, T. Amand, *Phys. Rev. B* **2013**, *88*, 121301.

[14] A. Castellanos-Gomez, R. Roldán, E. Cappelluti, M. Buscema, F. Guinea, H. S. J. van der Zant, G. A. Steele, *Nano Lett.* **2013**, *13*, 5361.

[15] Y. Wang, C. Cong, W. Yang, J. Shang, N. Peimyoo, Y. Chen, J. Kang, J. Wang, W. Huang, T. Yu, *Nano Res.* **2015**, *8*, 2562.

[16] A. P. Nayak, S. Bhattacharyya, J. Zhu, J. Liu, X. Wu, T. Pandey, C. Jin, A. K. Singh, D. Akinwande, J.-F. Lin, *Nat. Commun.* **2014**, *5*.

[17] W. Fan, X. Zhu, F. Ke, Y. Chen, K. Dong, J. Ji, B. Chen, S. Tongay, J. W. Ager, K. Liu, H. Su, J. Wu, *Phys. Rev. B* **2015**, *92*, 241408.

[18] Z. Zhao, H. Zhang, H. Yuan, S. Wang, Y. Lin, Q. Zeng, G. Xu, Z. Liu, G. K. Solanki, K. D. Patel, Y. Cui, H. Y. Hwang, W. L. Mao, *Nat. Commun.* **2015**, *6*.

[19] X. Dou, K. Ding, D. Jiang, X. Fan, B. Sun, *ACS Nano* **2016**, *10*, 1619.

[20] Z.-H. Chi, X.-M. Zhao, H. Zhang, A. F. Goncharov, S. S. Lobanov, T. Kagayama, M. Sakata, X.-J. Chen, *Phys. Rev. Lett.* **2014**, *113*, 036802.

[21] A. P. Nayak, Z. Yuan, B. Cao, J. Liu, J. Wu, S. T. Moran, T. Li, D. Akinwande, C. Jin, J.-F. Lin, *ACS Nano* **2015**, *9*, 9117.

[22] M. Peña-Álvarez, E. del Corro, Á. Morales-García, L. Kavan, M. Kalbac, O. Frank, *Nano Lett.* **2015**, *15*, 3139.

[23] A. P. Nayak, T. Pandey, D. Voiry, J. Liu, S. T. Moran, A. Sharma, C. Tan, C.-H. Chen, L.-J. Li, M. Chhowalla, J.-F. Lin, A. K. Singh, D. Akinwande, *Nano Lett.* **2015**, *15*, 346.

[24] Y. Y. Hui, X. Liu, W. Jie, N. Y. Chan, J. Hao, Y.-T. Hsu, L.-J. Li, W. Guo, S. P. Lau, *ACS Nano* **2013**, *7*, 7126.

[25] Z. Liu, M. Amani, S. Najmaei, Q. Xu, X. Zou, W. Zhou, T. Yu, C. Qiu, A. G. Birdwell, F. J. Crowne, *Nat. Commun.* **2014**, *5*.

[26] R. Rafael, C.-G. Andrés, C. Emmanuele, G. Francisco, *J. Phys. Condens. Matter* **2015**, *27*, 313201.

[27] C. Zheng, Z.-Q. Xu, Q. Zhang, M. T. Edmonds, K. Watanabe, T. Taniguchi, Q. Bao, M. S. Fuhrer, *Nano Lett.* **2015**, *15*, 3096.

[28] B. Zhu, X. Chen, X. Cui, *Sci. Rep.* **2015**, *5*, 9218.

[29] K. F. Mak, K. He, C. Lee, G. H. Lee, J. Hone, T. F. Heinz, J. Shan, *Nat. Mater.* **2013**, *12*, 207.

[30] A. Chernikov, A. M. van der Zande, H. M. Hill, A. F. Rigosi, A. Velauthapillai, J. Hone, T. F. Heinz, *Phys. Rev. Lett.* **2015**, *115*, 126802.

[31] H. Liu, J. Lu, K. Ho, Z. Hu, Z. Dang, A. Carvalho, H. R. Tan, E. S. Tok, C. H. Sow, *Nano Lett.* **2016**, *16*, 5559.

[32] M. S. Kim, S. J. Yun, Y. Lee, C. Seo, G. H. Han, K. K. Kim, Y. H. Lee, J. Kim, *ACS Nano* **2016**, *10*, 2399.

[33] M. Buscema, G. A. Steele, H. S. J. Zant, A. Castellanos-Gomez, *Nano Res.* **2015**, *7*, 561.

[34] K. Liu, Q. Yan, M. Chen, W. Fan, Y. Sun, J. Suh, D. Fu, S. Lee, J. Zhou, S. Tongay, *Nano lett.* **2014**, *14*, 5097.

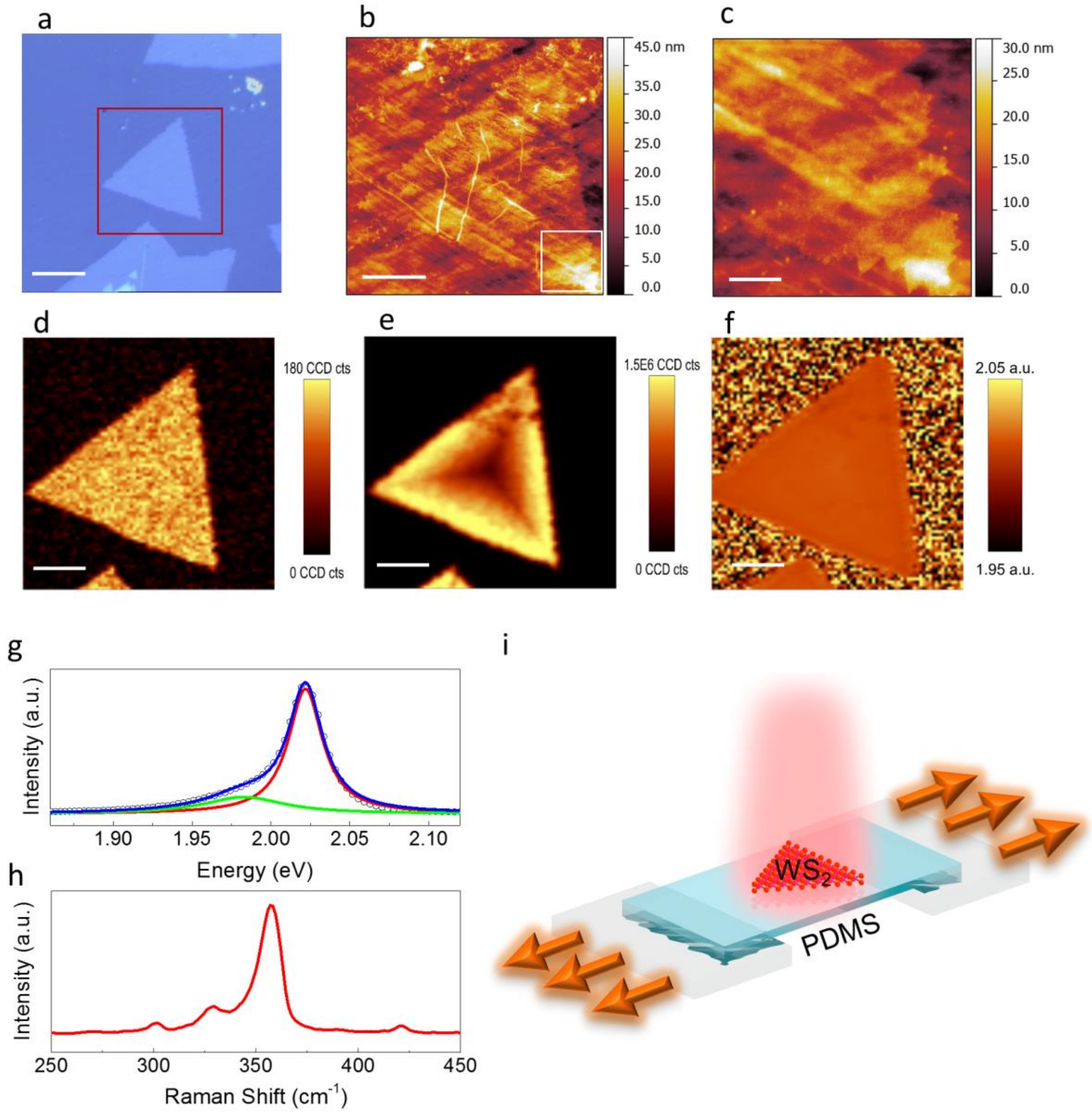

Figure 1. (a) Optical image of a WS_2 crystal transferred on PDMS substrate. (b) AFM height image of the WS_2 crystal on PDMS. (c) Height image of the square region shown in (b). (d-f) Integrated Raman intensity, integrated PL intensity and PL peak position mapping of the WS_2 crystal on PDMS. (g) PL spectrum of WS_2 on PDMS without strain. Black circles are experimental data; blue line is a fit to the

This article is protected by copyright. All rights reserved.

sum of two Lorentzians (red and green lines). (h) Raman spectrum of WS_2 on PDMS without strain. (i) Schematic of tensile stress loading frame. Scale bar: 5 µm in (a,b) and (d-f); 1 µm in (c).

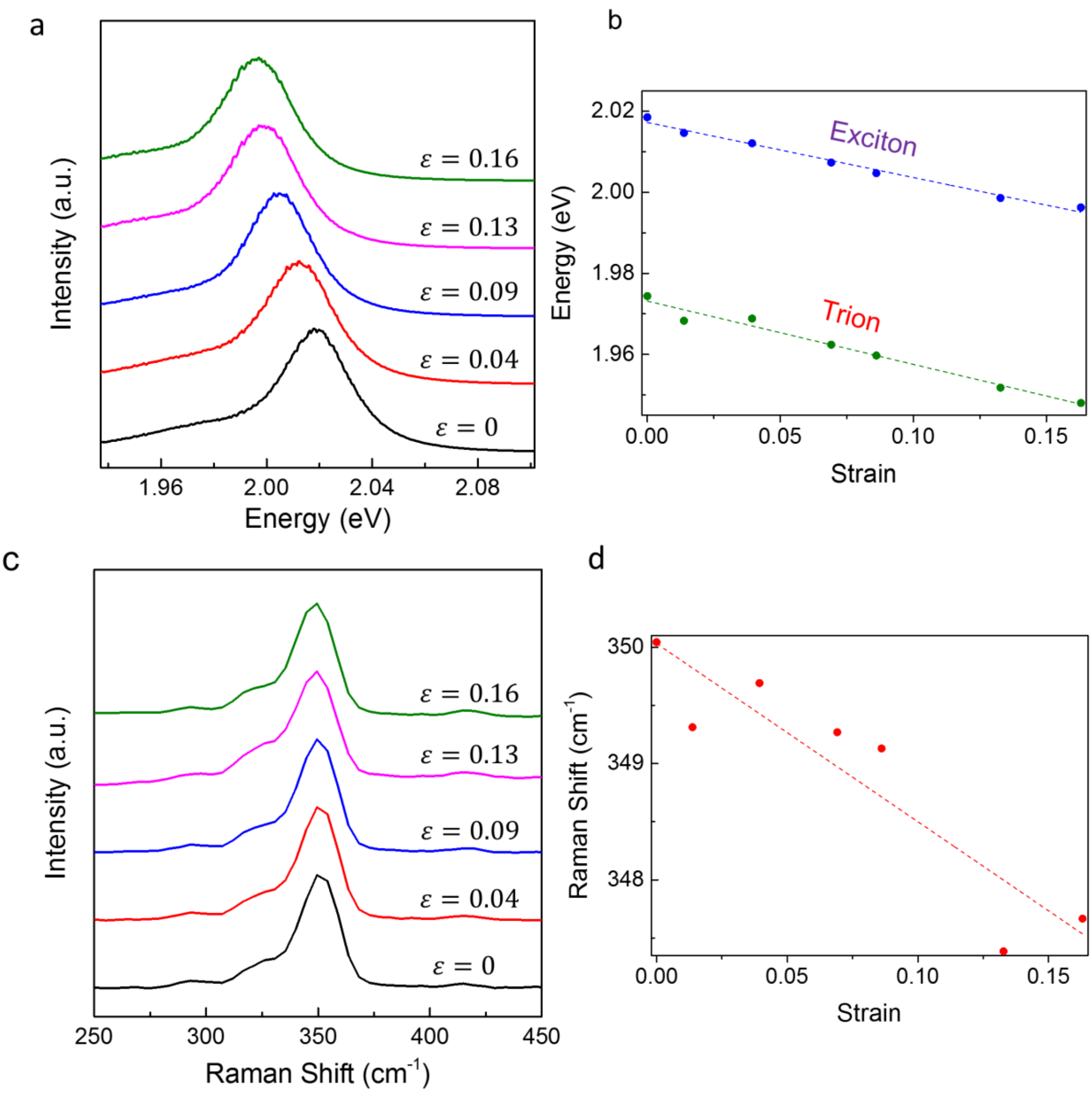

Figure 2. (a) Redshift of photoluminescence spectra of WS_2 on PDMS substrate as the PDMS strain increases from 0 to 0.16. (b) Evolution of the exciton (X^-) and trion (X^0) peak energies with strain. (c) Raman spectra of E' peak as PDMS strain increasing from 0 to 0.16. (d) Evolution of E' Raman

This article is protected by copyright. All rights reserved.

shift as a function of PDMS strain. The strain values given in the plots are tensile strain of PDMS substrate.

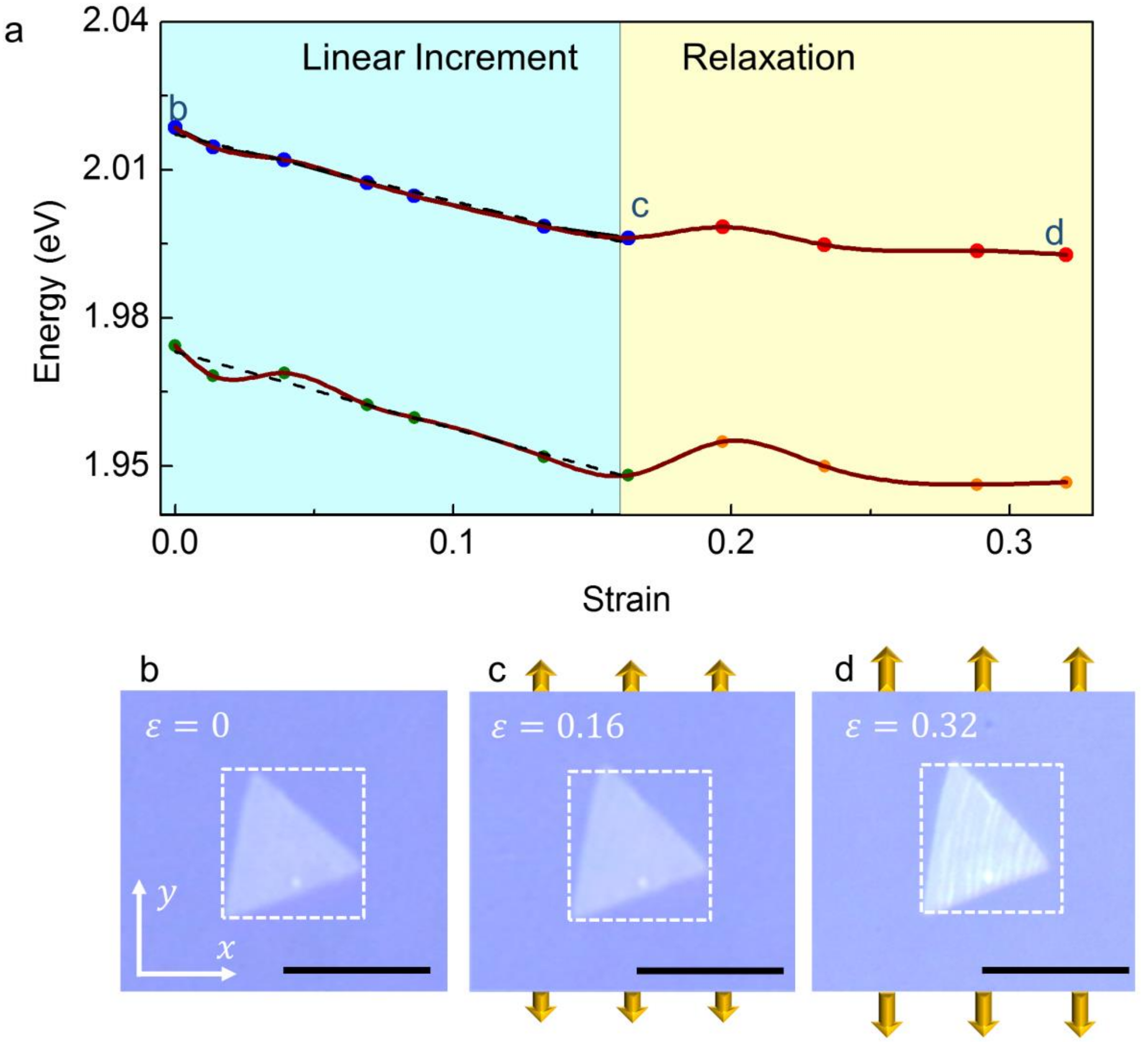

Figure 3. (a) Energies of X^- and X^0 photoluminescence peaks as a function of the PDMS tensile strain, showing two distinct regions. (b-d) Optical images of the WS$_2$ crystal at three typical points: (b) no strain, (c) 0.16 tensile strain, and (d) 0.32 tensile strain. The strain values given are tensile strain of PDMS substrate. Scale bar: 5 µm.

This article is protected by copyright. All rights reserved.

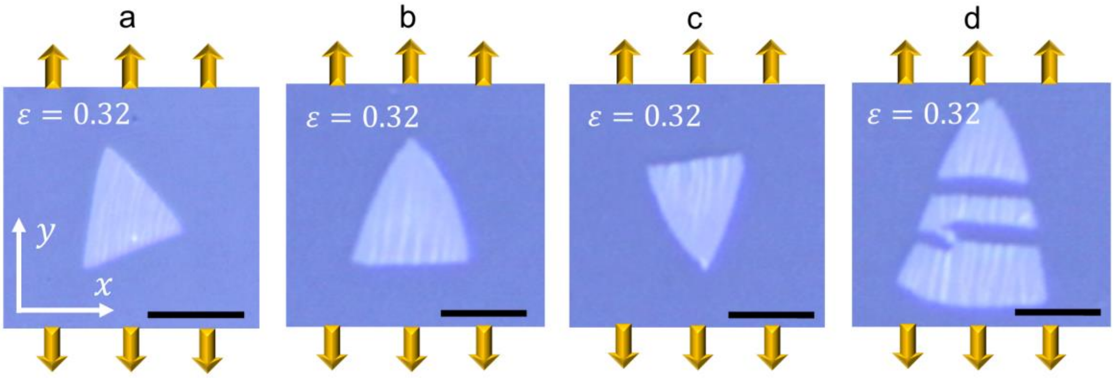

Figure 4. Optical images of WS_2 crystals with different orientations to the tensile strain direction and sizes at 0.32 PDMS strain. Scale bar: 5 µm.

This article is protected by copyright. All rights reserved.

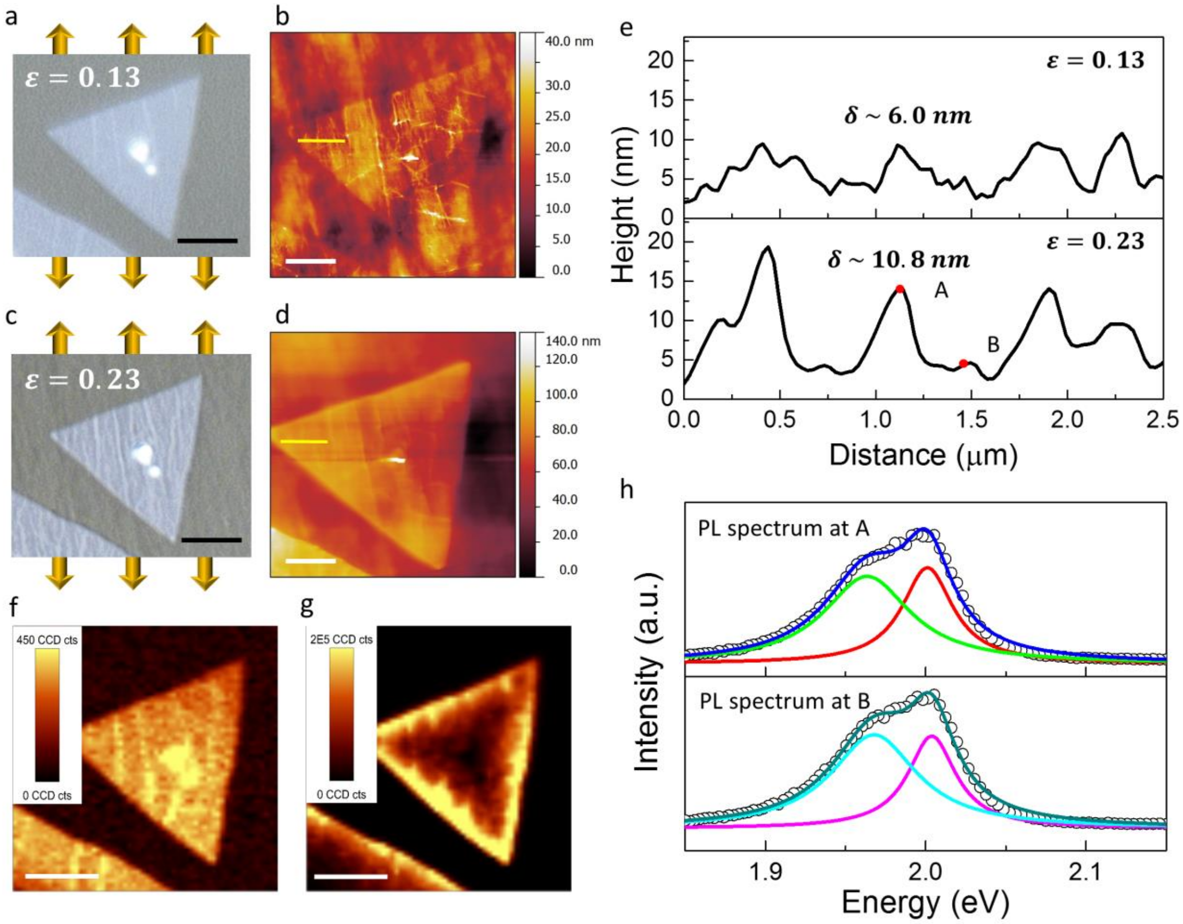

Figure 5. (a,b) Optical and AFM height images of WS_2 crystal with one edge parallel to tensile strain direction at 0.13 PDMS strain. (c,d) Optical and AFM height images of WS_2 crystal with one edge parallel to tensile strain direction at 0.23 PDMS strain. (e) Height profiles of WS_2 corresponding to

This article is protected by copyright. All rights reserved.

yellow lines in (b) (0.13 strain) and (d) (0.23 strain). (f,g) Integrated Raman and PL intensity mapping of the WS_2 crystal at 0.23 tensile strain. (h) PL spectra extracted at positions A and B in (g). Scale bar: 5 µm in (a), (c), (g) and (f); 3 µm in (b) and (d).

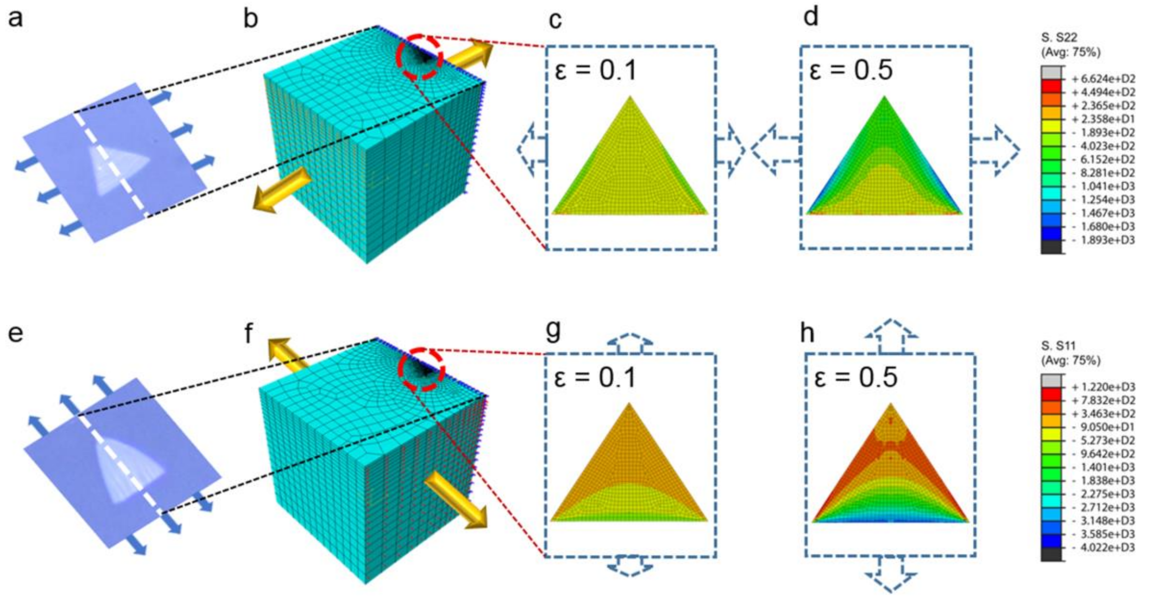

Figure 6. Finite element (FE) simulation of WS_2 under tensile strain. (a, b) FE model of WS_2/PDMS sample under tensile strain corresponding to the case in Figure 4(a). (c, d) Snapshots of FE simulation results of WS_2 under the substrate strain at 0.1 and 0.5. (e, f) FE model of WS_2/PDMS sample under tensile strain corresponding to the case in Figure 4(b, c). (g, h) Snapshots of FE simulation results of WS_2 under substrate strain at 0.1 and 0.5.

.

This article is protected by copyright. All rights reserved.

Table of Content

Strain relaxation with wrinkle formation is observed on monolayer WS_2 triangular crystals at high tensile strain. Raman and photoluminescence mapping, atomic force microscopy and finite element simulation are applied to investigate the characteristics of wrinkles. Our results reveal the distribution of wrinkles is highly dependent on the orientation of the triangle crystals relative to the tensile strain direction.

Keyword: Monolayers

Qianhui Zhang, Zhenyue Chang, Guanzhong Xu, Ziyu Wang, Yupeng Zhang, Zai-Quan Xu, Shujian Chen, Qiaoliang Bao, Jefferson Zhe Liu, Yui-Wing Mai, Wenhui Duan*, Michael S. Fuhrer*, Changxi Zheng*

Strain Relaxation of Monolayer WS_2 on Plastic Substrate

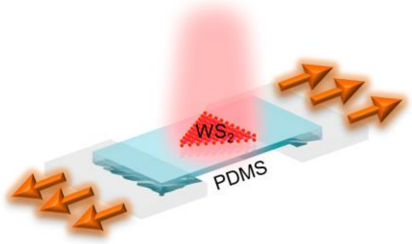

This article is protected by copyright. All rights reserved.